A Ship Detection and Tracking Algorithm for an Airborne Passive Interferometric Microwave Sensor (PIMS)

Hailiang Lu ⓘ, Hao Li, Liangbing Chen ⓘ, Yayun Cheng ⓘ, Dong Zhu ⓘ, *Member, IEEE*, Yinan Li, Rongchuan Lv, Gang Chen, Xiang Su, Liang Lang, Qingxia Li, and Yingying Zhao

Abstract—Ship detection by an airborne passive interferometric microwave sensor has been proposed as a powerful complementary tool for ship detection, especially for large ships in low visibility conditions and high sea clutter. In this article, the brightness temperature (TB) models of the sea background and the ship on the sea are established. Given the TB models, a ship detection and tracking algorithm with four steps is proposed, which is devoted to ship tracking. In addition, the impacts of the noises in the passive interferometric microwave images (PIMI) and the algorithm parameters are analyzed and discussed. Numerical simulations and airborne experiments are performed to assess the practicability of the algorithm. Both numerical and experimental results have demonstrated the practicability of the proposed algorithm with dealing with the additional systematic errors and estimating the ship heading, and the results also exhibit that the additional noises in the PIMI caused by the stochastic fluctuations of the aircraft and the algorithm parameters have a non-negligible impact on the algorithm detection performance. As a result, the "ship-free" observed TB maps should be carefully considered as the sea background TB map to improve the algorithm detection performance by reducing the noises caused by the stochastic fluctuations of the aircraft. In addition, the algorithm parameter should also be carefully considered to get a high ship detection probability with a low ship false-alarm rate.

Index Terms—Airborne, interferometric, microwave sensor, passive, ship detection and tracking.

Hailiang Lu, Hao Li, Yinan Li, Rongchuan Lv, Gang Chen, and Xiang Su are with the China Academy of Space Technology, Xi'an 710100, China (e-mail: hust_lhl@163.com; cast504_lihao@163.com; liyinan_cast@126.com; roselinda_lrc@163.com; 173536425@qq.com; gabriel1861@163.com).

Liangbing Chen is with the School of Information Engineering, Nanchang University, Nanchang 330031, China (e-mail: liangbingchen@gmail.com).

Yayun Cheng is with the Department of Engineering Physics, Tsinghua University, Beijing 100084, China (e-mail: chengyy915@163.com).

Dong Zhu is with the Department of Electronic Engineering, Tsinghua University, Beijing 100084, China (e-mail: zhudong@mail.tsinghua.edu.cn).

Liang Lang, Qingxia Li, and Yingying Zhao are with the School of Electronic Information and Communications, Huazhong University of Science and Technology, Wuhan 430074, China (e-mail: l_lang@mail.hust.edu.cn; qingxia_li@hust.edu.cn; 839812850@qq.com).

Digital Object Identifier 10.1109/JSTARS.2021.3066514

I. INTRODUCTION

SHIP detection from the airborne/spaceborne platforms is of vital importance and has a wide array of applications, such as traffic surveillance and management, oil-spill detection, fishery management, and illegal smuggling [1], [2]. In recent years, the main airborne/spaceborne sensors for ship detection are automatic identification systems [3], [4], optical sensors [5], infrared sensors [6], [7], synthetic aperture radars (SAR), and so on [8], [9]. However, these sensors have their advantages and also have their weaknesses, especially in low visibility conditions and/or high sea clutter [10]–[15].

In [16], Lu *et al.* have proposed that ships on the sea are detected by an airborne passive interferometric microwave sensor (PIMS), which can be considered as a powerful complementary tool for ship detection, especially for large ships in low visibility conditions and high sea clutter. Airborne experiments have also demonstrated that ships on the sea can be effectively detected by an airborne PIMS in sunny weather and cloudy weather [16]. In comparison with the optical and infrared sensors, ship detection by the airborne PIMS has efficient imaging capability in low visibility conditions. In comparison with SARs, ship detection by the airborne PIMS has no speckle issue and slightly suffers from sea clutter, and so on [17]. Therefore, the aforementioned sensors can complement each other for ship detection in all weather and all day conditions.

For an airborne PIMS, ship detection is based on the high contrast of the ships on the sea in the passive interferometric microwave image (PIMI). For example, the metallic ship on the sea always exhibits a high contrast with a "cold" brightness temperature (TB) characteristic in the PIMI [13]. In [16], a ship detection algorithm has been proposed to detect the ships on the sea for the airborne PIMS, in which only the systematic noises are considered. However, for an airborne PIMS, the residual additional systematic errors [22] and the noises caused by the fluctuations of the aircraft always exist in the PIMI, that will weaken or merge the high contrast of the ships in the PIMI and have negative impacts on the ship detection by an airborne PIMS. However, the mentioned residual additional systematic errors and noises caused by the fluctuations of the aircraft are not considered and analyzed in the ship detection algorithm proposed by [16].
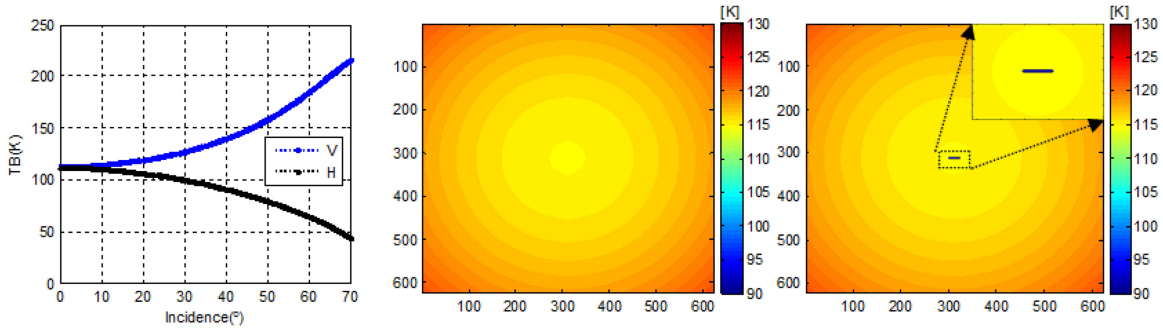
Fig. 1.　(Left) Sea surface TBs as a function of the incidence angle at V polarization (the blue dotted line) and H polarization (the black dotted line). (Middle) TB map of the sea surface at V Polarization. (Right) Apparent TB map of a metallic ship on the sea.

In this article, a ship detection and tracking algorithm is proposed, in which the residual additional systematic errors and the noises caused by the fluctuations of the aircraft are considered and analyzed. The ship detection and tracking algorithm cannot only accurately detect the ships, but also consecutively track the ships, as well as estimate the ship heading. The article is devoted to ship tracking and the impact of the noises caused by the fluctuations of the aircraft on the ship detection and tracking algorithm in contrast to the proposed algorithm in [16].

The remainder of this article is organized as follows. In Section II, the TB models of the sea background and the ship on the sea are analyzed and established. Following that, a ship detection and tracking algorithm is introduced and discussed for an airborne PIMS in Section III, and numerical simulations are performed in Section IV. Then, airborne experiments are performed, and results and discussions are given in Section V. Finally, the conclusion is drawn.

II. TB MODELS OF THE SEA BACKGROUND AND THE SHIP

In this section, the TB models of the sea background and the ship on the sea are analyzed and established.

A. TB Model of the Sea Background

It is well known that the self-emitted TB of sea surface at microwaves depends on sea surface salinity (SSS), sea surface temperature (SST), incidence angle, polarization, etc. [18], [19]. Thus, the self-emitted TB of sea surface at a given frequency can be expressed as a function as

$$\mathrm{TB_{SE}^{sea}} = e^{\mathrm{sea}}(\mathrm{SSS, SST,} \theta, \phi, p) \cdot \mathrm{SST} \qquad (1)$$

where e^{sea} denotes the sea surface emissivity, which is also a function of SSS, SST, incidence angle, polarization, etc. θ denotes the incidence angle, ϕ denotes the azimuth angle, and p denotes the V or H polarization. The self-emitted TB of sea surface can also be expressed in the direction cosines $(\xi, \eta) = (\sin\theta\cos\phi, \sin\theta\sin\phi)$. For the open ocean, SSS and SST are almost the same within the range of tens of kilometers or even hundreds of kilometers. As a result, the self-emitted TB of sea surface at each polarization has a dependence on the incidence angles in the open ocean, which is nearly the same within the same incidence angle. As shown in Fig. 1 (left), the self-emitted TB of sea surface as a function of the incidence angles in an open

ocean with 32 psu SSS and 300 K SST at 10.7 GHz are given at V polarization (blue dotted line) and H polarization (black dotted line), respectively. For the incidence angle ranging from 0° to 70°, the self-emitted TB of sea surface increases as the incidence angle increases at V polarization, but it decreases as the incidence angle increases at H polarization.

For an airborne PIMS in the ideal case, the apparent TB of sea surface can be expressed as

$$\mathrm{TB_{AP}^{sea}} = \mathrm{TB_{SE}^{sea}} \cdot \tau_{\mathrm{Up}} + T_{\mathrm{DN}} \cdot (1 - e^{\mathrm{sea}}) \cdot \tau_{\mathrm{Up}} + T_{\mathrm{UP}} \qquad (2)$$

where τ_{UP} denotes the transmissivity between the sea surface and the airborne PIMS, T_{DN} denotes the down-welling atmospheric radiation, and T_{UP} denotes the up-welling atmospheric radiation between the sea surface and the airborne PIMS. As shown in Fig. 1(middle), the apparent TB of sea surface at V polarization is given. It can be seen that the apparent TB of sea surface is the same within the same incidence angle in the ideal case, as expected. However, for an airborne PIMS, the fluctuations of the aircraft are inescapable, and the incidence angle varies with the fluctuations of the aircraft. Thus, the observed TB of sea surface by the airborne PIMS will vary as the fluctuations of the aircraft.

For an airborne PIMS, the systematic errors can be corrected by the internal and/or the external calibration method [20], [21]. However, the residual systematic errors still exist in the observed TB maps, which are considered to be additive and called the residual additional systematic errors, such as in MIRAS [22]. In addition, the systematic noises should also be considered in the observed TB maps. Thus, the nth observed TB map of the sea background by an airborne PIMS can be expressed in the direction cosines (ξ, η) as

$$\mathrm{TB_{map}^{sea}}(\xi, \eta, n) = \mathrm{TB_{AP}^{sea}}(\xi, \eta, n) + \Delta T_{\mathrm{sys}}(\xi, \eta, n)$$
$$+ T_n(\xi, \eta) \qquad (3)$$

where ΔT_{sys} denotes the residual additional systematic errors or the additional systematic errors and T_n denotes the systematic noise in the PIMI. In the airborne PIMI, the residual additional systematic errors are considered to be additive and almost the same in the all frames that $\Delta T_{\mathrm{sys}}(\xi, \eta, 1) = \cdots = \Delta T_{\mathrm{sys}}(\xi, \eta, n) = \Delta T_{\mathrm{sys}}(\xi, \eta)$, such as in MIRAS [19].

Since the sea surface TB varies smoothly within tens of kilometers in the open ocean, the adjacent apparent TB maps

of the sea surface from the air are also considered to be almost the same:

$$\text{TB}_{\text{AP}}^{\text{sea}}(\xi, \eta, n) \approx \text{TB}_{\text{AP}}^{\text{sea}}(\xi, \eta, m), \quad \text{when } |m - n| < l \quad (4)$$

where l denotes the maximal length between the adjacent TB frames. However, the observed TB of sea surface by an airborne PIMS will be affected by the fluctuations of the aircraft and the airborne PIMS drift. In fact, the sea surface TB in an open ocean can be considered to be almost the same within tens of kilometers, and the TB variations of the sea surface TB are far slower than the TB variations caused by the fluctuations of the aircraft and the airborne PIMS drift. The airborne PIMS drift about several minutes or tens of minutes is slower than the fluctuations of the aircraft about several seconds. It means the observed TB variations caused by the fluctuations of the aircraft are faster than those caused by the airborne PIMS drift. As a result, l mainly depends on the fluctuations of the aircraft.

B. TB Model of the Ship on the Sea

As mentioned in [13], the ships on the sea are usually made of painted metals, such as oil tankers and container ships. The emissivity of a painted metallic ship is usually lower than 0.1 below 100 GHz. The apparent TB of a painted metallic ship can be expressed as

$$\text{TB}_{\text{Ap}}^{\text{ship}} = e^{\text{ship}} \cdot T^{\text{ship}} \cdot \tau_{\text{Up}} + T_{\text{DN}} \cdot (1 - e^{\text{ship}}) \cdot \tau_{\text{Up}} + T_{\text{UP}} \quad (5)$$

where e^{ship} denotes the emissivity of ship surface, T^{ship} denotes the physical temperature of the ship. As shown in Fig. 1(right), the apparent TB map of the painted metallic ship on the sea is given. The apparent TB of the painted metallic ship is smaller than 90 K from the airborne PIMS. It can be seen that the metallic ship exhibits a high contrast with a "cold" TB characteristic against the sea background in the PIMI.

In the airborne PIMI, a metallic ship can be considered as a point target or a line target [16]. Thus, the nth TB map model of sea surface with a metallic ship on the sea can also be expressed as

$$
\begin{aligned}
\text{TB}_{\text{map}}^{\text{ship}}(\xi, \eta, n) \\
= \text{TB}_{\text{AP}}^{\text{sea}}(\xi, \eta, n) + \Delta T_{\text{sys}}(\xi, \eta, n) + T_n(\xi, \eta, n) \\
+ (\text{TB}_{\text{AP}}^{\text{ship}}(\xi, \eta, n) - \text{TB}_{\text{AP}}^{\text{sea}}(\xi, \eta, n)) \cdot \delta(\xi - \xi_0, \eta - \eta_0)
\end{aligned}
\quad (6)
$$

where (ξ_0, η_0) denotes the pixel of the ship on the sea in the PIMI and δ is the impulse function. In (6), the TB map model of a metallic ship on the sea is established, in which the apparent TB of the metallic ship is lower than the apparent TB maps of the sea surface. However, the TB map model of the objects with small radar signatures on the sea can also be expressed by (6), such as wooden materials and fiberglass materials. The objects with small radar signatures also exhibit a high contrast with a "hot" TB characteristic against the sea background in the PIMI [23]. In addition, when the object is a line target or a face target, the TB model of the objects in (5) and (6) is also established that (ξ_0, η_0) is a pixel set.
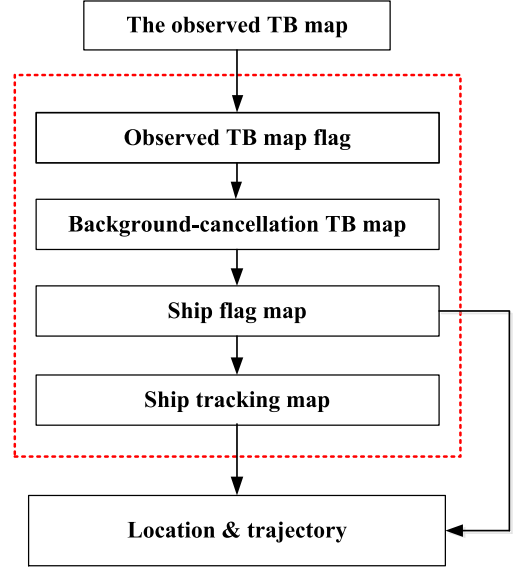

Fig. 2. Flowchart of the ship detection and tracking algorithm.

III. SHIP DETECTION AND TRACKING ALGORITHM FOR AN AIRBORNE PIMS

This section is devoted to a ship detection and tracking algorithm, and the impacts of the noises on the algorithm are analyzed and discussed.

A. Ship Detection and Tracking Algorithm

The ship detection and tracking algorithm consists of four steps that the observed TB map flag, the background-cancellation TB map, the ship flag map, and the ship tracking map, as shown in Fig. 2. In contrast to the algorithm in [16], the residual additional systematic errors are considered by step 1 $\sim$ step 3 in the proposed algorithm, which satisfies the realistic condition for the airborne PIMS.

Step 1. Observed TB map flag

The first step aims at preliminarily flagging the observed TB maps with ships. We assume that a ship is located at the pixel (ξ_0, η_0) in the nth observed TB map and the ship is located at the pixel (ξ_1, η_1) in the mth observed TB map. For the two observed TB maps, the difference-detection TB map can be defined and expressed as

$$
\begin{aligned}
\Delta T_{\text{DD}}(\xi, \eta, n) &= \text{TB}_{\text{map}}^{\text{ship}}(\xi, \eta, n) - \text{TB}_{\text{map}}^{\text{ship}}(\xi, \eta, m) \\
&= (\text{TB}_{\text{AP}}^{\text{ship}}(\xi_0, \eta_0, n) - \text{TB}_{\text{AP}}^{\text{sea}}(\xi_0, \eta_0, n)) \\
&\quad - (\text{TB}_{\text{AP}}^{\text{ship}}(\xi_1, \eta_1, m) - \text{TB}_{\text{Ap}}^{\text{sea}}(\xi_1, \eta_1, m)) \\
&\quad + \sqrt{2} T_n(\xi, \eta).
\end{aligned}
\quad (7)
$$

Since the noise $T_n(\xi, \eta)$ in each observed TB map is additive and stochastic, the noise in the difference-detection TB map (7) is $\sqrt{2} T_n(\xi, \eta)$. Then, the observed TB map flag is performed

based on the difference-detection TB maps as follows:

$$f(n) = \begin{cases} 1, & if \quad \max\{|\Delta T_{\mathrm{DD}}(\xi, \eta, n)|\} \geq N \cdot \sigma_0 \\ 0, & else \end{cases} \quad (8)$$

in which "1" denotes that ships exist in the nth observed TB maps (called as "ship-existing" observed TB maps) and "0" denotes no ships exist in the nth observed TB maps (called as "ship-free" observed TB maps), N is a scaling threshold factor and a variable parameter, and σ_0 is the standard deviation of the observed TB maps with matched loads in the internal calibration method. When there is a ship in the field of view of the airborne PIMS, the consecutive "ship-existing" observed TB maps $(t_1, \ldots, t_s)$ will be flagged as "1" in the step.

Step 2. Background-cancellation TB map

The background-cancellation TB map is the difference between the "ship-existing" observed TB maps and the "ship-free" observed TB maps in step 1, which can be expressed as

$$\Delta T_{\mathrm{BC}}(\xi, \eta, n) = \mathrm{TB}_{\mathrm{map}}^{\mathrm{ship}}(\xi, \eta, n) - \mathrm{TB}_{\mathrm{map}}^{\mathrm{sea}}(\xi, \eta, k)$$
$$= (\mathrm{TB}_{\mathrm{AP}}^{\mathrm{ship}}(\xi_0, \eta_0, n) - \mathrm{TB}_{\mathrm{AP}}^{\mathrm{sea}}(\xi_0, \eta_0, n))$$
$$+ \sqrt{2} T_n(\xi, \eta) \quad (9)$$

where the kth observed TB map is the sea background in which there is no ship.

Step 3. Ship flag map

The metallic ships always exhibit a "cold" TB characteristic in the PIMI, so the ship flag map is performed as

$$\mathrm{Flag}(\xi, \eta, n) = \begin{cases} 1, & \Delta T_{\mathrm{BC}}(\xi, \eta, n) \leq -M \cdot \sigma_0 \\ 0, & \Delta T_{\mathrm{BC}}(\xi, \eta, n) > -M \cdot \sigma_0 \end{cases} \quad (10)$$

in which "1" denotes that there are ships in the pixels (called as "ship-existing" pixels), "0" denotes that there are no ships in the pixels (called as "ship-free" pixels), $M \cdot \sigma_0$ is the threshold, and M is also a scaling threshold factor and a variable parameter. Since the parameter N in Step 1 is used to preliminarily determine the frame range of the "ship-existing" observed TB maps and the parameter M in Step 3 is used to flag the ship in the background-cancellation TB map, M is assigned to be not smaller than N in our algorithm.

Step 4. Ship tracking map

In Step 3, the "ship-existing" pixels are flagged as "1" in the background-cancellation TB maps, and the location of the ship in the "ship-existing" observed TB maps can also be estimated. Since the ship sails continuously on the sea, the ship tracking map can be estimated by the consecutive ship flag maps by using "and" operation as follows:

$$\mathrm{Track}(\xi, \eta) = \sum_{n=t_1}^{t_s} \mathrm{Flag}(\xi, \eta, n). \quad (11)$$

In fact, the ship tracking map is the relative trajectory of the detected ship with respect to the aircraft, and the trajectory of the aircraft can be estimated by the airborne sensors. In our algorithm, the ship on the sea can be accurately detected and
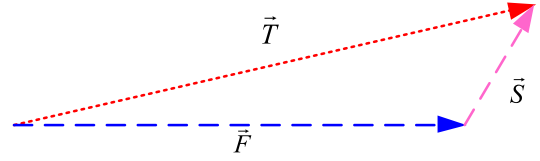

Fig. 3. Relationships between the relative trajectory $\vec{T}$ of the ship, the trajectory $\vec{F}$ of the aircraft, and the ship vector $\vec{S}$.

consecutively tracked, and the location and relative trajectory of the detected ship can be also estimated. In the ideal case, this trajectory is continuous in the PIMI with respect to the aircraft.

In addition, the ship heading and/or ship speed can be also estimated by the location and relative trajectory of the detected ship. As shown in Fig. 3, the relative trajectory of the ship $(\vec{T})$ and the trajectory of the aircraft $(\vec{F})$ are given. The ship vector $(\vec{S})$ (the ship heading and speed) can be estimated by

$$\vec{S} = \vec{T} - \vec{F}. \quad (12)$$

In addition, since the objects with low radar signatures exhibit a "hot" TB characteristic in the PIMI, the objects with low radar signatures can also be accurately detected and consecutively tracked using the ship detection and tracking algorithm by just adjusting (10) as follows:

$$\mathrm{Flag}(\xi, \eta, n) = \begin{cases} 1, & \Delta T_{\mathrm{BC}}(\xi, \eta, n) \geq M \cdot \sigma_0 \\ 0, & \Delta T_{\mathrm{BC}}(\xi, \eta, n) < M \cdot \sigma_0. \end{cases} \quad (13)$$

In comparison to the algorithm in [16], the proposed algorithm mainly focuses on ship tracking and ship heading.

B. Impact of the Algorithm Parameter and the Noise

The ship detection probability and ship false-alarm rate (FAR) are two key specifications to assess the algorithm detection performance. In the ship detection and tracking algorithm, the ship detection probability is defined as the ratio of the observed TB maps with ship pixels correctly flagged as "1" to the total observed TB maps of the ship within the field of view of the airborne PIMS, and FAR is defined as the ratio of the observed TB maps with "ship-free" pixels falsely flagged as "1" to the total observed TB maps of the ship within the field of view of the airborne PIMS. In this subsection, the impacts of the algorithm parameter and the noises on the algorithm detection performance are analyzed.

1) Impact of the Algorithm Parameter M and Noises: In the ship detection and tracking algorithm, the ship detection probability and ship FAR depend on the signal-to-noise ratio (SNR) of the ship to the sea background in the PIMI [16].

In accordance with (9), the SNR of the detected ship in the background-cancellation TB maps can be defined as

$$\mathrm{SNR} = \frac{\left| \mathrm{TB}_{\mathrm{AP}}^{\mathrm{ship}}(\xi_0, \eta_0, n) - \mathrm{TB}_{\mathrm{AP}}^{\mathrm{sea}}(\xi_0, \eta_0, n) \right|}{\sqrt{2} \sigma(T_n(\xi, \eta))} \quad (14)$$

in which $\sigma(T_n(\xi, \eta))$ denotes the standard deviation of the noises $T_n(\xi, \eta)$ in the observed TB maps.

When there is a ship in the observed TB map, and the "ship-existing" pixels in the background-cancellation TB map is flagged as "1" by (10) in Step 3, the relationship between $\Delta T_{BC}(\xi,\eta,n)$ and $M \cdot \sigma_0$ can be expressed as

$$|\Delta T_{\rm BC}(\xi, \eta, n)| \geq M \cdot \sigma_0. \qquad (15)$$

Equation (9) is substituted into (15)

$$\left| {\rm TB}_{\rm AP}^{\rm ship}(\xi_0, \eta_0, n) - {\rm TB}_{\rm AP}^{\rm sea}(\xi_0, \eta_0, n) + \sqrt{2}T_n(\xi, \eta) \right|$$
$$\geq M \cdot \sigma_0. \qquad (16)$$

Then, an unequal equation is obtained

$$\left| {\rm TB}_{\rm AP}^{\rm ship}(\xi_0, \eta_0, n) - {\rm TB}_{\rm AP}^{\rm sea}(\xi_0, \eta_0, n) \right|$$
$$+ \sqrt{2}\left| \sigma(T_n(\xi, \eta)) \right| \geq M \cdot \sigma_0. \qquad (17)$$

Equation (17) is substituted into (14), the defined SNR of the detected ship in the background-cancellation TB maps is expressed as follows:

$$\text{SNR} \geq \frac{M \cdot \sigma_0}{\sqrt{2}\sigma(T_n(\xi, \eta))} - 1. \qquad (18)$$

The ship detection probability and ship FAR depend on SNR [16]. However, in accordance with (18), the defined SNR in (14) depends on the noises $T_n(\xi, \eta)$ in (9) and the algorithm parameter M in (10). Hence, one can know that the noises in (9) and the algorithm parameter M in (10) will have a non-negligible impact on the detection performance of the proposed algorithm in terms of the ship detection probability and ship FAR.

2) Impact of Noises Caused by the Fluctuations of the Aircraft: For an airborne PIMS, the observer angle between the airborne PIMS and the sea surface varies with the fluctuations of the aircraft. It means that the incidence angle also varies with the fluctuations of the aircraft. That will leads to some discrepancies between the sea background TB maps that ${\rm TB}_{\rm AP}^{\rm sea}(\xi, \eta, n) \neq {\rm TB}_{\rm AP}^{\rm sea}(\xi, \eta, k)$ in (9). As a result, the additional noises will be added to the background-cancellation TB maps that

$$\Delta T_f(\xi, \eta) = \left| {\rm TB}_{\rm AP}^{\rm ship}(\xi, \eta, n) - {\rm TB}_{\rm AP}^{\rm sea}(\xi, \eta, k) \right|. \qquad (19)$$

In this case, the background-cancellation TB map in (9) is expressed as

$$\Delta T_{BC}(\xi, \eta, n) = {\rm TB}_{\rm AP}^{\rm ship}(\xi_0, \eta_0, n) - {\rm TB}_{\rm AP}^{\rm sea}(\xi_0, \eta_0, n)$$
$$+ \sqrt{2}T_n(\xi, \eta) + \Delta T_f(\xi, \eta). \qquad (20)$$

Then, the defined SNR of the detected ship in the background-cancellation TB map can be redefined as

$$\text{SNR} = \frac{\left| {\rm TB}_{\rm AP}^{\rm ship}(\xi_0, \eta_0, n) - {\rm TB}_{\rm AP}^{\rm sea}(\xi_0, \eta_0, n) \right|}{\sigma(\sqrt{2}(T_n(\xi, \eta)) + \Delta T_f(\xi, \eta))}. \qquad (21)$$

In comparison to (14), the additional noises in (21) caused by the fluctuations of the aircraft will degrade the SNR, and the degraded SNR will reduce the algorithm detection performance. Thus, the observed TB maps of the sea background should be carefully selected for each ship in Step 2 to reduce the impact of the fluctuations of the aircraft on the algorithm detection performance by minimizing the additional noise in (19).

In addition, as mentioned in [16] and [23], ship wakes always also exhibit a high contrast with a "hot" TB characteristic against the sea background in the PIMI from the air. As a result, ship wakes can also be considered as another distinct characteristic to detect the sailing ship. In addition, ship heading can be estimated based on the "cold" TB characteristics and the "hot" TB characteristics of the sailing ship. Since the proposed algorithm is devoted to the "cold" TB characteristic of the ship, in which the "hot" TB characteristic of the ship wakes is not considered, ship wakes will be considered to further enhance the algorithm detection performance in the further works.

IV. NUMERICAL SIMULATIONS

In this section, numerical simulations are performed to verify the practicability of the algorithm and assess the impacts of the noises and the parameters on the algorithm detection performance.

In the numerical simulations, SSS is 32 psu, SST is 300 K, and the object is a sailing metallic ship with 230 m length and 32 m width. The weather is sunny and the atmospheric attenuation is also considered.

A. Ship Detection and Tracking Algorithm

In the numerical simulations, the proposed algorithm is performed to detect and track the sailing metallic ship from an airborne X-band PIMS at 10 km altitude. An example is shown in Fig. 4. The X-band apparent TB map of the sea surface at the altitude of 10 km is shown in Fig. 4(a). The X-band apparent TB map of the metallic ship on the sea is shown in Fig. 4(b). The observed TB maps of the ship by the X-band PIMS at t1 and at the next time t2 are shown in Fig. 4(c) and (d), respectively, in which both the noises $T_n(\xi, \eta)$ and the residual additional systematic errors $\Delta T_{\rm sys}$ are considered with $\sigma(T_n(\xi, \eta)) = 2$ K and $\sigma(\Delta T_{\rm sys}) = 2$ K. The difference-detection TB map of Fig. 4(c) and (d) by Step 1 with $N = 3$ and $\sigma_0 = 2$ K is shown in Fig. 4(e). The background-cancellation TB map of Fig. 4(c) by Step 2 is shown in Fig. 4(f). The ship flag map of Fig. 4(c) by Step 3 with $M = 3$ is shown in Fig. 4(g). Finally, the ship tracking map of the metallic ship by Step 4 is shown in Fig. 4(h), in which the colorbar denotes the number of "ship-existing" pixels through ship flag maps. As shown in Fig. 4, it can be seen that the sailing metallic ship can be accurately detected and consecutively tracked by the proposed algorithm. The numerical results indicate that the proposed algorithm is practical. In addition, the results also indicate that the proposed algorithm can deal with the residual systematic errors, as expected. It means that only the multiplicative errors that the amplitude and phase errors [20] are needed to be calibrated for ship detected by an airborne PIMS.

B. Impact of the Algorithm Parameter M

As aforementioned, the algorithm parameter M has a non-negligible impact on the algorithm detection performance. Numerical simulations are performed to assess the impact of the parameter M on the algorithm detection performance in terms of the ship detection probability and ship FAR. As the same conditions in Fig. 4, numerical simulations are performed with
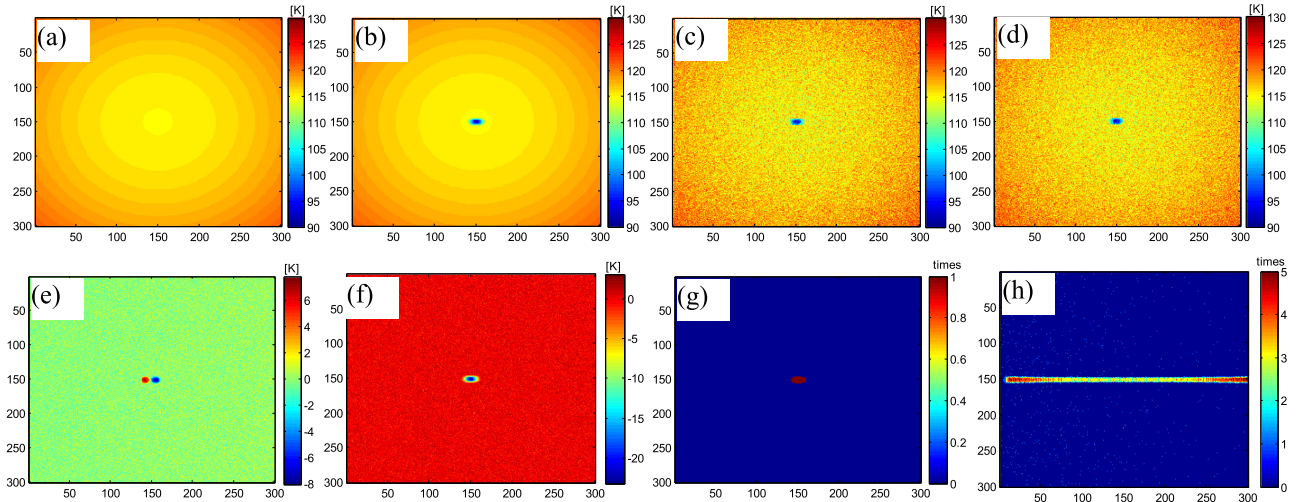
Fig. 4. Example that a metallic ship detected by the ship detection and tracking algorithm. (a) X-band apparent TB map of the sea surface at the altitude 10 km. (b) X-band apparent TB map of the metallic ship on the sea. (c) Ship TB map obtained by the X-band PIMS at t1 with considering the noises caused by the systematic noises and the fluctuations of the atmospheric, and the additional residual instrumental systematic errors. (d) Ship TB map obtained by the X-band PIMS at t2 as in (c). (e) Difference-detection TB map between (c) and (d) by Step 1. (f) Background-cancellation TB maps of (c) by Step 2. (g) Ship flag map of Fig. 4 (c) by Step 3. (h) Ship tracking map of the metallic ship by Step 4, in which the colorbar denotes the number of "ship-existing" pixels through ship flag maps.
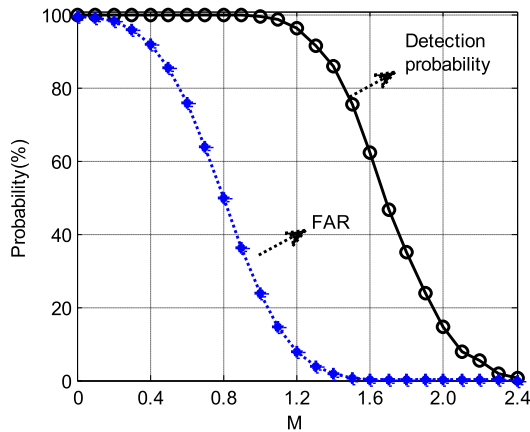
Fig. 5. Ship detection probability (black circle line) and ship FAR (blue dotted line) vs the algorithm parameter M.

Fig. 6. Curves of the ship detection probability as the ship FAR with $\sigma(T_n(\xi, \eta)) = 2, 3, 4, 5, 6,$ and 7 K in the PIMI.

the algorithm parameter M ranging from 0 to 2.4 with 0.1 steps for 1000 times. The ship detection probability and ship FAR vs the algorithm parameter M ($N = M$) are calculated and shown in Fig. 5. It can be seen that the algorithm parameter M has an important impact on the algorithm detection performance that the ship detection probability and ship FAR decrease as the algorithm parameter M increases. However, a high ship detection probability with a low FAR is expected in the ship detection. Thus, a compromise should be made for the algorithm parameter M to get a high ship detection probability with a low FAR, such as $M = 1.2$ in Fig. 5.

C. Impact of the Noises $T_n(\xi, \eta)$ in the PIMI

As aforementioned, the noises $T_n(\xi, \eta)$ in the PIMI also have a non-negligible impact on the algorithm detection performance. Numerical simulations are also performed to access the impact
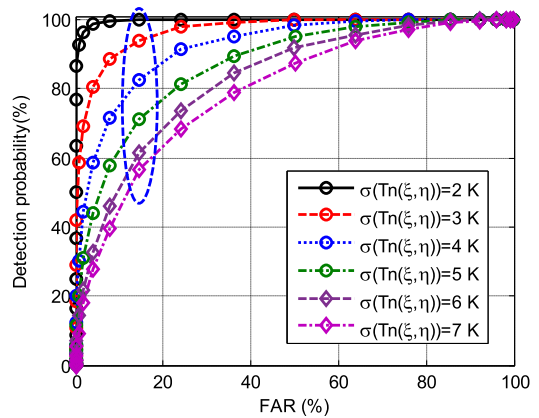
of noises $T_n(\xi, \eta)$ in the PIMI on the algorithm detection performance, in which the algorithm parameter setting is the same as that in Fig. 4. The ship detection probability and ship FAR are calculated by performing the numerical simulations at the algorithm parameter M also ranging from 0 to 2.4 with 0.1 steps for 1000 times with $\sigma(T_n(\xi, \eta)) = 2, 3, 4, 5, 6,$ and 7 K, respectively. Fig. 6 depicts the curves of the ship detection probability as the ship FAR with $\sigma(T_n(\xi, \eta)) = 2, 3, 4, 5, 6,$ and 7 K, respectively. It can be seen that the ship detection probability increases as the noise $\sigma(T_n(\xi, \eta))$ decreases at a constant ship FAR, as the blue dotted ellipse in Fig. 6. The results indicate the noises have a negative impact on the algorithm detection performance that the higher the noises in the PIMI, the lower the ship detection probability at a constant ship FAR. By (14) and (21), it can be deduced that the additional noises in (21) caused by the fluctuations of the aircraft also have a negative impact on the algorithm detection performance.

Fig. 7. (Left) Aircraft and (right) X-band PIMS in the experiments.
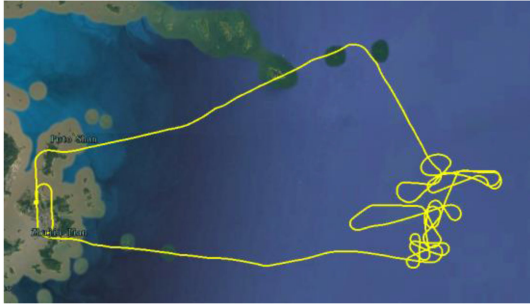

Fig. 8. Flight route (yellow line) of the aircraft in one experiment.

V. EXPERIMENTS, RESULTS, AND DISCUSSIONS

To verify the practicability and assess the performance of the ship detection and tracking algorithm, airborne experiments are performed by an X-band PIMS, as shown in Fig. 7(left). The X-band PIMS comprises a "Y-shaped" antenna array, as shown in Fig. 7(right). The inner six antenna elements in each arm and the hub element (total 19 antenna elements) are connected with the receivers, and the residual antenna elements in each arm are not connected with the receivers to keep the consistency of the antenna patterns for the inner six antennas in each arm and the hub element [see Fig. 7(right)]. The -3 dB beam-width of each antenna is about $65°$, the center frequency is 10.65 GHz, and the bandwidth is 100 MHz. The integration time is 100 ms, which can be adjusted as needed. In the airborne experiments, the X-band PIMS is installed on the bottom of the aircraft shown in Fig. 7(left), and an optical camera is also installed on the bottom of the aircraft to record the observation scenes for the data analysis.

In the airborne experiments, first, the external calibration method is performed to calibrate the multiplicative errors that the amplitude and phase errors of the X-band PIMS [16], [24], which are multiplicative errors. After that, the fast fourier transform (FFT) and the absolute calibration are performed to obtain the observed TB maps of the sea scene [25]. Due to the low angular resolution of the X-band PIMS that about $7.2°$ in the blackman window, all the observed TB maps are retrieved by FFT with three-time zero-padded. In the airborne experiments, the aircraft flies randomly over the sea to detect the ships by the X-band PIMS. As the yellow line shown in Fig. 8, the flight route of the aircraft in one day is given. In the airborne experiments, the
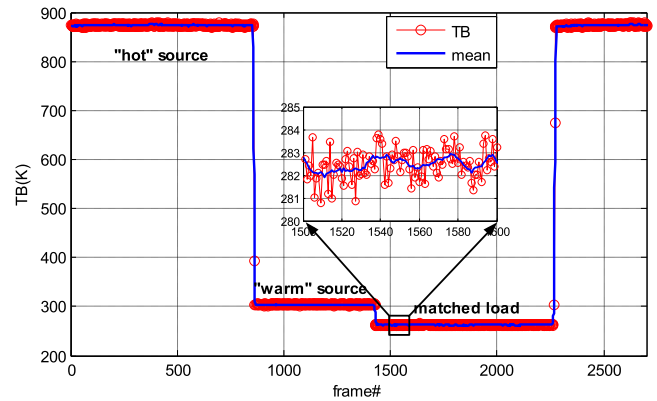

Fig. 9. Observed TB (red dotted line) and moving-averaged observed TB mean (blue line) of the hub element in the internal calibration.
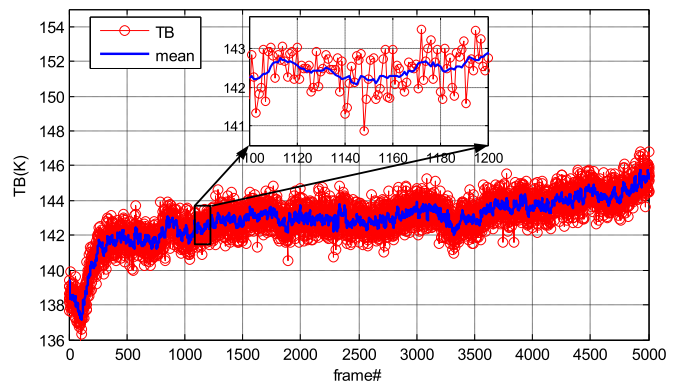

Fig. 10. Observed TB (red dotted line) and moving-averaged observed TB mean (blue line) of the hub elements from the open sea to coastal areas.

altitude of the aircraft is about 900 m, and the spatial resolution of the X-band PIMS is about 110 m at the altitude.

A. Stochastic Fluctuations of the Aircraft

As mentioned in Section III-B, the noises caused by the fluctuations of the aircraft have a non-negligible impact on the algorithm detection performance. Thus, the noises caused by the fluctuations of the aircraft are analyzed and discussed before performing the ship detection and tracking algorithm.

Since the fluctuations of the aircraft are more obvious and easily analyzed in the TB of one element (considered as a real-aperture microwave passive sensor) than the X-band PIMS, the hub element in the X-band PIMS is considered to analyze the fluctuations of the aircraft, which is the center one in the "Y-shape" antenna array, as the red circle in Fig. 7(right). As shown in Fig. 9, the observed TB (red dotted line) and moving-averaged observed TB mean (blue line) of the hub element in the X-band PIMS are given, when the calibration switch in the calibration subsystem is connected to the "hot" source, "warm" source, and matched loads, respectively [24]. For comparison, the observed TB (red dotted line) and moving-averaged observed TB mean (blue line) of the hub element in the X-band PIMS are also shown in Fig. 10, when the aircraft flies over an open sea with no ships.
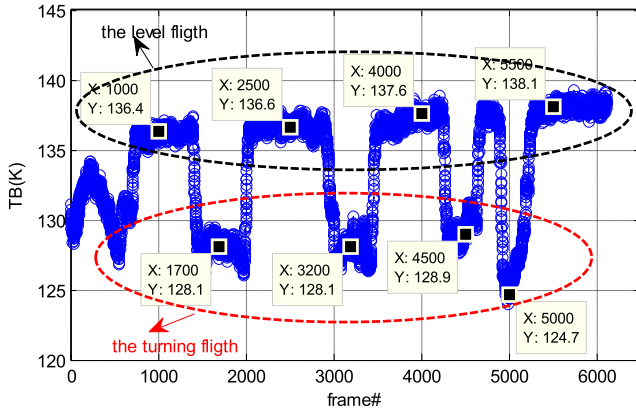
Fig. 11. Observed TB of the hub element in one airborne experiment.

Fig. 12. Footprints of the aircraft on the sea surface in the level flight (black dotted circles) and the turning flight (red dotted circles).

In the airborne experiments, the receivers' noise temperature of the X-band PIMS varies slowly, which has a dependence on the environment temperature. Without considering the fluctuations of the aircraft, the standard deviation between the observed TB and the moving-averaged observed TB mean of the hub element is equal to the system sensitivity of the hub element. Thus, the standard deviation between the observed TB and the moving-averaged observed TB mean of the hub element can be estimated by [26]:

$$\sigma_{\text{cal or sea}} = \frac{T_A + T_R}{\sqrt{B \cdot \tau}} \quad (22)$$

in which T_A is the antenna temperature or the internal calibration noise temperature, T_R is the receiver noise temperature, B is the system bandwidth, and τ is the integration time. For the X-band PIMS, the integration time, the system bandwidth, and the receiver's noise temperature are the same in the airborne experiments.

In the airborne experiments, the noise temperature of "warm" source is about 300 K, which is higher than the antenna temperature (about $130 \sim 180$ K) of the sea scene. By (22), the standard deviation σ_{load} of matched loads (see Fig. 9) should also be higher than the standard deviation σ_{sea} of the sea scene (see Fig. 10) without considering the fluctuations of the aircraft. It is known that the standard deviation σ_{load} of matched loads in the hub element is not affected by the fluctuations of the aircraft. However, in the airborne experiments, the standard deviation σ_{load} (about 0.65 K) of matched loads in the hub element in Fig. 9 is smaller than the standard deviation σ_{sea} (about 0.71 K) of the hub element of the sea scene in Fig. 10. The results demonstrate that the fluctuations of the aircraft have produced additional noises in the TB of the hub element. It also means that the fluctuations of the aircraft will produce additional noises in the observed TB maps, as expected.

As shown in Fig. 11, the observed TB of the hub element of the X-band PIMS is given in one airborne experiment. It is found that there are large discrepancies in the observed TB of the hub element between the large black dotted ellipse and the red dotted ellipse in Fig. 11. By analyzing the sensor (GPS+SPAN) of the aircraft and the optical im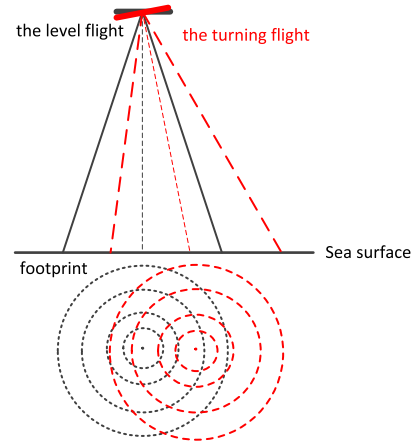ages, the large discrepancies are caused by the turning of the aircraft to observe the ship on the sea. As shown in Fig. 12, the footprints of the hub element on the sea surface are given in the level flight (black dotted circles) and the turning flight (red dotted circles), respectively. Since the X-band PIMS operates at H-polarization, the observed TB of the sea surface at H-polarization decreases as the incidence angle increases. In the turning flight, the footprint of the hub element has more regions within the large incidences, as the red dotted circle shown in Fig. 12. Thus, the observed TB of the hub element decreases as the turning flight of the aircraft.

The observed TB maps of the X-band PIMS are also analyzed for the airborne experiments in Fig. 13. As shown in Fig. 13 (top), four observed TB maps of the X-band PIMS in the level flight that frame#1000, frame#2500, frame#4000, and frame#5500 (see Fig. 11) are given. Meanwhile, as shown in Fig. 13(bottom), four observed TB maps of the X-band PIMS in the turning flight that frame#1700, frame#3200, frame#4500, and frame#5000 (see Fig. 11) are also given. As shown in Fig. 13, it is found that there are large discrepancies between the observed TB maps of the X-band PIMS in the level flight [see Fig. 13(top)] and the turning flight [see Fig. 13(bottom)]. Meanwhile, it is also found that there is also a small discrepancy between the observed TB maps of the X-band PIMS in the level flight [see Fig. 13(top)], which are caused by the additional noises caused by the stochastic fluctuations of the aircraft. The additional noises will reduce the high contrast of the detected ship in the background-cancellation TB maps to reduce the SNR of the detected ship in the background-cancellation TB map and degrade the algorithm detection performance. Thus, the sea background TB map should be carefully selected to reduce the additional noises caused by the fluctuations of the aircraft. In addition, the additional systematic errors also exist in each observed TB map due to only the external calibration method performed in the airborne experiments to calibrate the multiplicative errors [16]. Otherwise, the observed TB maps should be almost the same within the incidence angles, similar as Fig. 1(middle). Meanwhile, the systematic noises also exist in the observed TB maps, such as Fig. 13.
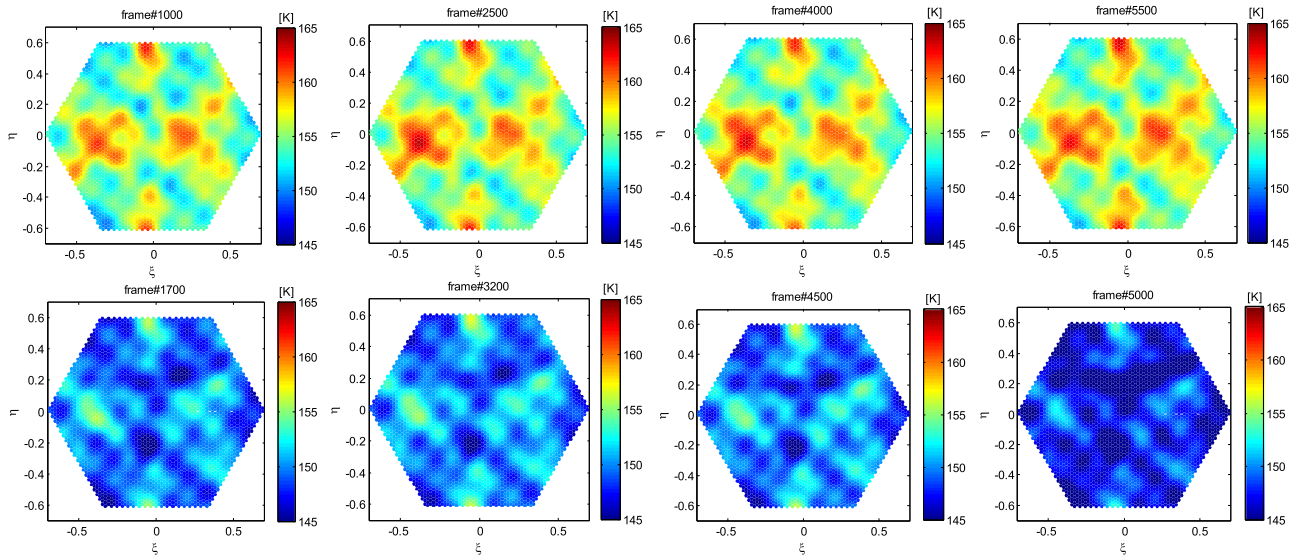
Fig. 13. Four observed TB maps of the X-band PIMS in the level flight (top) and the turning flight (bottom), respectively.

TABLE I
FRAME RANGE OF SEVERAL CONSECUTIVE TB MAP SETS FLAGGED AS "1" IN
ONE AIRBORNE EXPERIMENT

No.	Frame range
Ship.1	$2420 \sim 2500$
Ship.2	$2220 \sim 2350$
Ship.3	$5600 \sim 5810$
Ship.4	$1140 \sim 1270$
Ship.5	$4040 \sim 4140$

B. Experimental Results

The ship detection and tracking algorithm is performed to the airborne experiment shown in Fig. 11. First, Step 1 is performed with $N \cdot \sigma_0 = 1.0$ K, and several consecutive observed TB map sets are flagged as "1." The frame ranges of several consecutive "ship-existing" observed TB map sets are given in Table I. As shown in Fig. 14(a), two "ship-existing" observed TB maps that frame#2430 and frame#2460 of Ship 1 in Table I are given, and the difference-detection TB maps of the observed TB maps by Step 1 with $|n-m| = 10$ are also shown in Fig. 14(b). In the airborne experiments, l in (4) mainly depends on the fluctuations of the aircraft, which can be analyzed and assessed by the TB of the hub element (see Figs. 10 and 11). By analyzing the TB fluctuations of the hub element in Figs. 10 and 11, $|n - m|$ is designed to be 10 in Step 1. Following that, Step 2 is performed, and the background-cancellation TB maps of the "ship-existing" observed TB maps are shown in Fig. 14(c), in which the "ship-free" observed TB maps that frame#2100 is carefully selected as the sea background $\mathrm{TB}^{\mathrm{sea}}_{\mathrm{map}}(\xi, \eta, k)$ in (9) by analyzing the TB fluctuations of the hub element in Figs. 11 and 15. As shown in Fig. 15, the frame ranges of Ship 1 and Ship 2 are given, as the black rectangles. Since the "ship-free" observed TB maps selected as the sea background should be the same as the "ship-existing" observed TB maps within the frame range of the detected ships in Fig. 15 as possible, frame#2100 is

selected as the sea background in Fig. 14 for Ship 1. Then, Step 3 is performed with $M \cdot \sigma_0 = 1.3$ K, and the ship flag maps of the "ship-existing" observed TB maps are given in Fig. 14(d). As shown in Fig. 14(d), it can be seen that a ship is flagged in the ship flag maps. As shown in Fig. 14(c), there is a "low" TB region in the background-cancellation TB maps. As mentioned in Section II, the "low" TB region should be a metallic ship. Thus, the "low" TB region in the background-cancellation TB maps [see Fig. 14(c)] is flagged as "1" in Fig. 14(d) by Step 3. For comparison, the optical images are also shown in Fig. 14(e). It is also found that there is indeed a metallic ship on the sea in each optical image [see Fig. 14(e)], in which the location of the ship on the sea is the same as the "low" TB region in the background-cancellation TB maps [see Fig. 14(c)] and the "ship-existing" pixels in the ship flag maps [see Fig. 14(d)].

The residual background-cancellation TB maps and the ship flag maps of Ship 1 are also obtained by Step 2 and Step 3. The "low" TB region in each background-cancellation TB map and the corresponding "ship-existing" pixels in each ship flag map are also demonstrated to be a metallic ship by the optical images. Finally, the ship tracking map of Ship 1 is estimated by Step 4, as shown in Fig. 16(top). The detection algorithm is also performed to Ship 2 and Ship 3 in Table I, and the ship tracking maps are also shown in Fig. 16(middle) and (bottom), respectively. In addition, ship heading estimated by the algorithm is shown in Fig. 16, as the pink arrows. The results reveal that there is indeed a metallic ship in the "ship-existing" observed TB maps flagged as "1" by the ship detection and tracking algorithm, which are also demonstrated by the optical images, such as the black diamond in Fig. 16. The ship heading has been demonstrated by the latitude/longitude and magnetic angles. As shown in Fig. 17, the longitude/latitude and the magnetic angle of the aircraft are given for the airborne experiment shown in Fig. 11. The ship tracking map can be translated into the earth-centered earth-fixed reference using the position and attitude of the aircraft by compensating the dynamics of the aircraft. The experimental

(a)
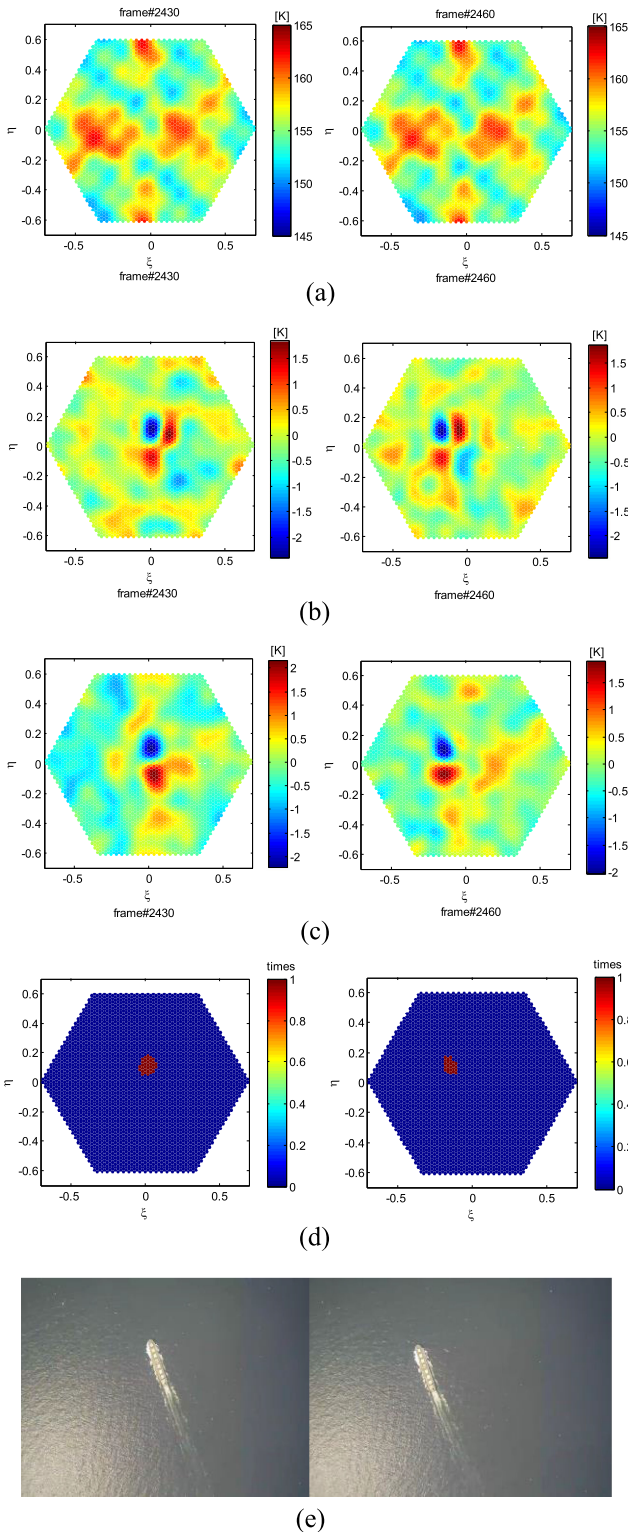

(b)

(c)

(d)

(e)

Fig. 14. (a) Two observed TB maps that frame#2430 and frame#2460 of Ship 1 in Table I. (b) Difference-detection TB maps of the observed TB maps in Fig. 14(a) by Step 1 with $N \cdot \sigma_0 = 1.0$ K and $|n-m| = 10$. (c) Background-cancellation TB maps of the observed TB maps in Fig. 14(a) by Step 2, in which frame#2100 is considered as the sea background TB map. (d) Ship flag maps of the observed TB maps in Fig. 14(a) by Step 3 with $M \cdot \sigma_0 = 1.3$ K. (e) Optical images of two observed TB maps in Fig. 14(a).
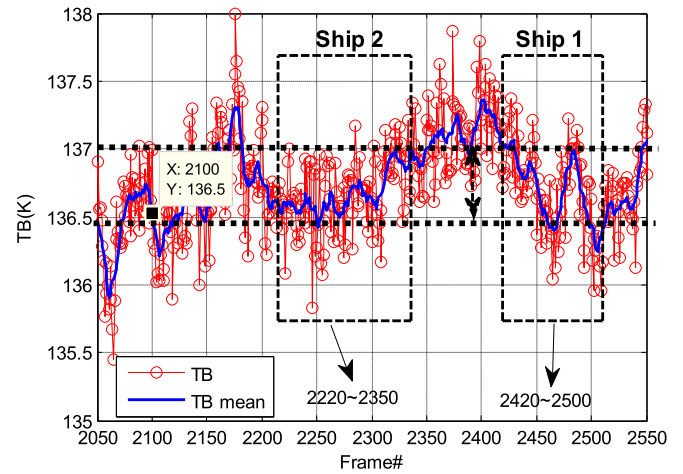

Fig. 15. TB (red dotted line) and moving-averaged TB mean (blue line) of the hub elements for Ship 1 and Ship 2.

results indicate that the algorithm is practical and the ships can be accurately detected and consecutively tracked by the algorithm. Meanwhile, the experimental results also indicate that the ship heading can be accurately estimated by the algorithm.

Since only the multiplicative errors of the X-band PIMS are corrected by the external calibration method in the airborne experiments, the additional systematic errors of the X-band PIMS exist in the observed TB maps, such as Figs. 13 and 14(a). However, the ships can also be accurately detected and consecutively tracked by the algorithm in the airborne experiments. That also indicates that the algorithm can deal with the additional systematic errors, as expected.

In addition, it is also found that the "low" TB region in the background-cancellation TB maps [such as Fig. 14(c)] is always accompanied by a "high" TB region, which is caused by ship wakes. The TB characteristic of ship wakes is also mentioned in [13].

C. Impact of the Noise and the Algorithm Parameter M

In this subsection, the impacts of the noises and the algorithm parameter M on the algorithm detection performance are analyzed by the airborne experiments.

1) Impact of the Noises Caused by the Stochastic Fluctuations of the Aircraft: As aforementioned, the "ship-free" observed TB maps should be carefully considered as the sea background TB map in Step 2 to reduce the impact of the stochastic fluctuations of the aircraft on the algorithm detection performance. As shown in Fig. 18, the background-cancellation TB maps, the ship flag maps and the ship tracking maps of the "ship-exiting" observed TB map that frame#2430 [see Fig. 14(a)] are given with $M \cdot \sigma_0 = 1.3$ K, in which the "ship-free" observed TB maps that frame#1000, frame#1700, frame#4000, and frame#4500 (see Fig. 11) are selected as the sea background TB map, respectively. In these cases, the detection probability and FAR of Ship 1 are counted and given in Table II. As shown in Fig. 18 and Table II, it can be seen that the "ship-free" observed TB maps in the turning flight (frame#1700
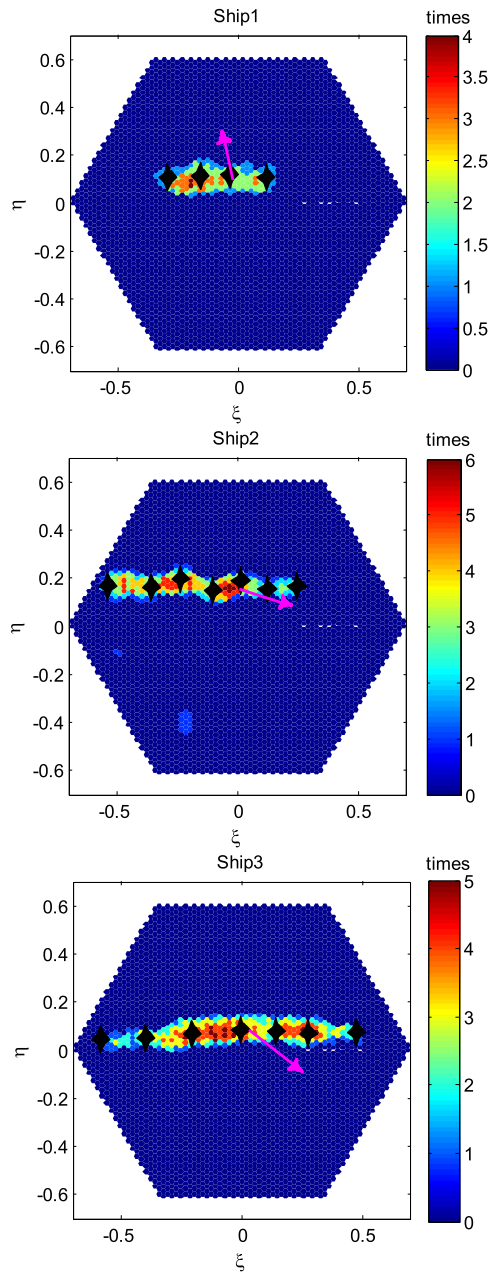
Fig. 16. Ship tracking maps of Ship1 (top), Ship2 (middle), and Ship3 (bottom) in Table I detected by the ship detection and tracking algorithm.
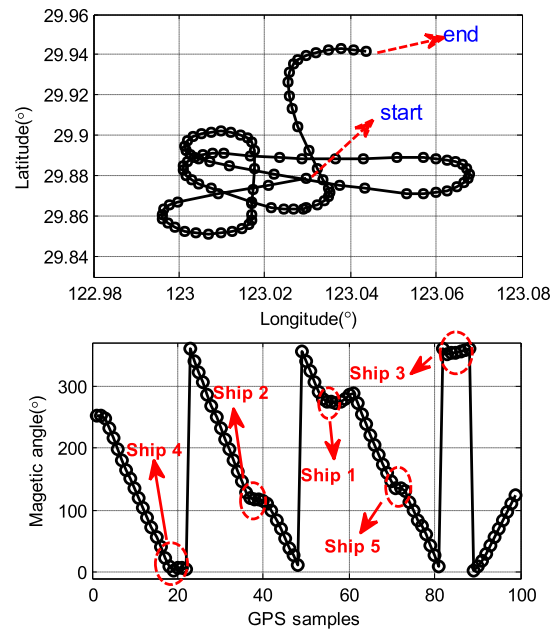

Fig. 17. Longitude/latitude (top) and the magnetic angle (bottom) of the airborne experiment in Fig. 11.

TABLE II
DETECTION PROBABILITY AND FAR OF SHIP 1 IN TABLE I IN DIFFERENT SEA BACKGROUND WITH $M \cdot \sigma_0 = 1.3$ K

Frame#	Detection Probability	FAR
1000	67%	0%
1700	0%	0%
4000	100%	0%
4500	0%	0%
2100	100%	0%

and frame#4500) considered as sea background TB maps show a greatly reduced performance. It is also found that the "ship-free" observed TB maps in the level flight (frame#1000, frame#4000, and frame#2100) considered as sea background TB maps exhibit different characteristics in the background-cancellation TB maps and the ship flag maps [see Fig. 18(top) and (middle)], and they also exhibit different detection performances in terms of the ship detection probability and FAR [see Table II and Fig. 18(bottom)]. The results exhibit that the "ship-free" observed TB maps should be carefully considered as the sea background TB map to improve the algorithm detection performance by reducing the additional noises in (19), which is caused by the fluctuations of the aircraft.

2) Impact of the Algorithm Parameter M: As mentioned in Section III, the algorithm parameter *M* also has a non-negligible impact on the algorithm detection performance. The impact of the algorithm parameter *M* is also analyzed and discussed in terms of the ship detection probability and the ship FAR in the airborne experiments. The standard deviation σ_0 of the TB maps with matched loads in (11) and (15) is about 0.65 K.

In the airborne experiments, many ships are accurately detected and consecutively tracked by the proposed algorithm. As shown in Fig. 19, the ship tracking maps of two examples that Ship 2 and Ship 3 in Table I are given with $M \cdot \sigma_0 = 1.6$, 1.2, 0.8, and 0.4 K, respectively. It is found that some "ship-free" pixels in the ship tracking map are falsely flagged as ships, such as $M \cdot \sigma_0 = 1.2$ K in Ship 2 and $M \cdot \sigma_0 = 0.8$ in Ship 3, and many "ship-free" pixels in the ship tracking map are falsely flagged as ships, such as $M \cdot \sigma_0 = 0.8$ and 0.4 K in Ship 2 and $M \cdot \sigma_0 = 0.4$ in Ship 3. The results indicate that the "ship-free" pixels falsely flagged as "ship-existing" pixels increase as the algorithm parameter *M* decreases.

In addition, the statistics of the ship detection probability and the ship FAR for the detected ships is also performed with different algorithm parameter $M \cdot \sigma_0$ in the airborne experiments. As shown in Fig. 20, the ship detection probability and ship FAR
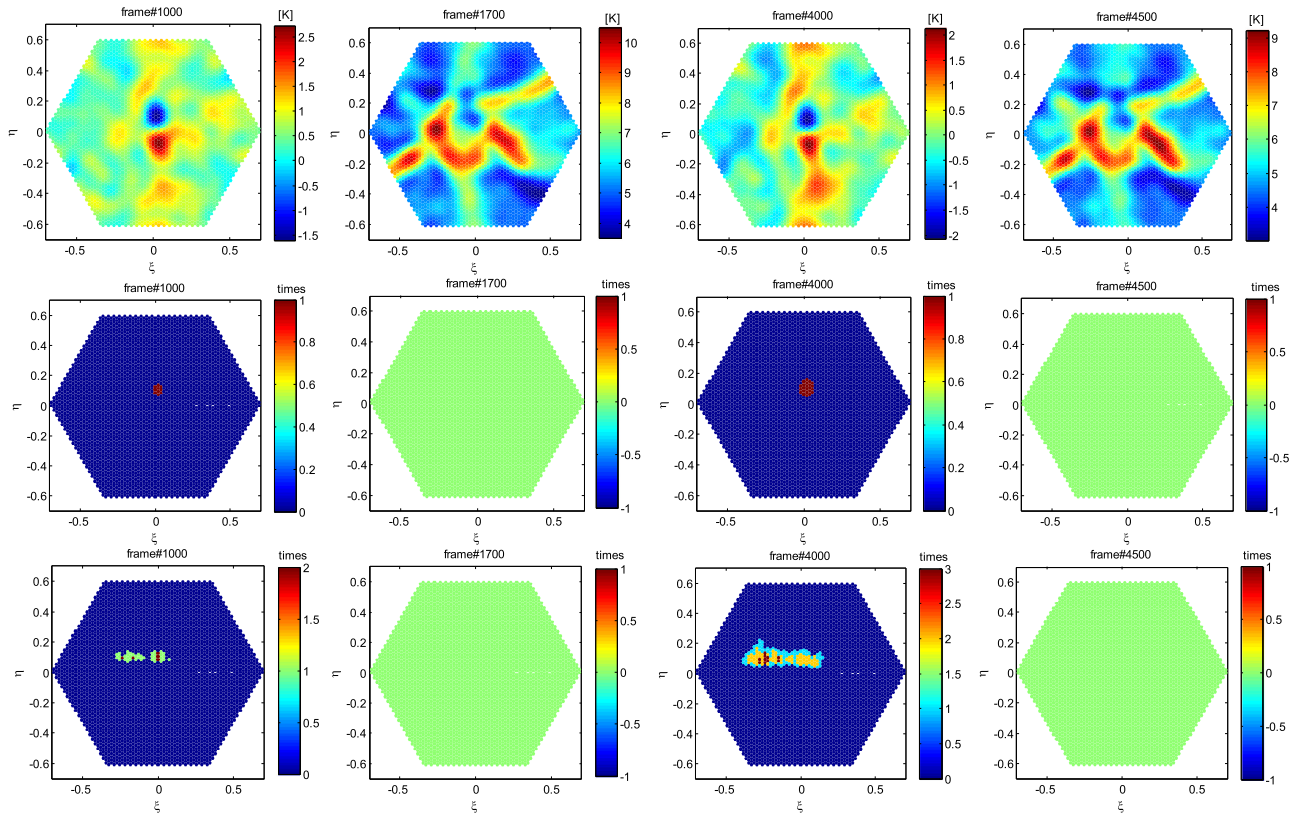
Fig. 18. Background-cancellation TB maps (top), the ship flag maps (middle), and the ship tracking maps (bottom) of frame#2430 in Fig. 9(a) by performing the ship detection and tracking algorithm with $M \cdot \sigma_0 = 1.3$ K, in which frame #1000, frame #1700, frame #4000, and frame #4500 (from left to right) are considered as the sea background map, respectively.
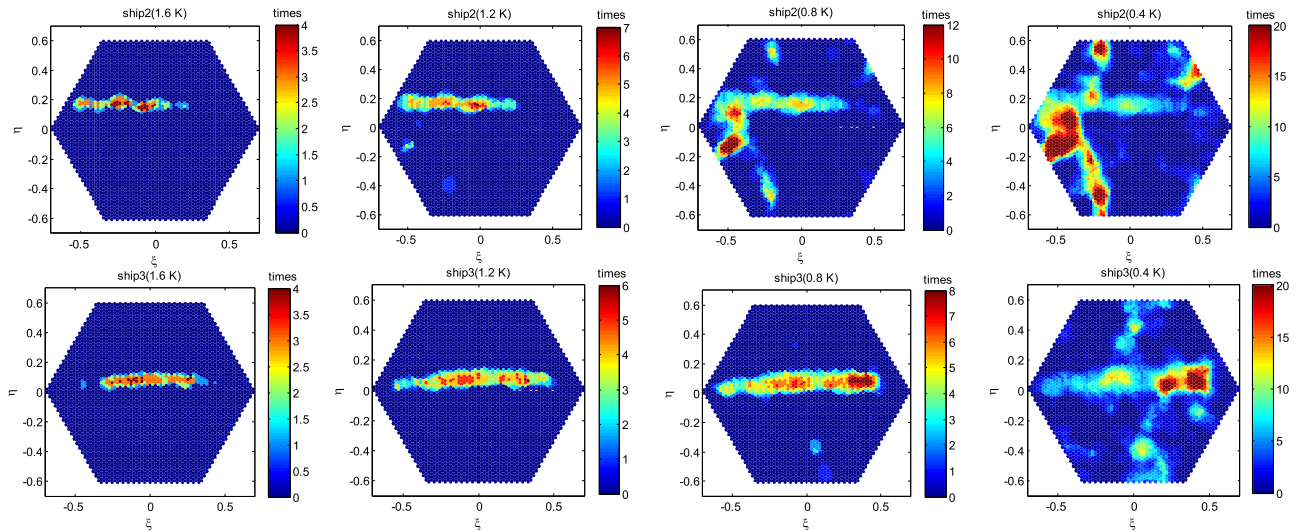

Fig. 19. Ship tracking maps of Ship 2 (top) and Ship 3 (bottom) in Table I when $M \cdot \sigma_0 = 1.6$, 1.2, 0.8, and 0.4 K (from left to right).

of Ship 2 (top) and Ship 3 (bottom) in Table I as a function of the algorithm parameter $M \cdot \sigma_0$ ($\sigma_0 = 0.65$ K) are given, respectively. It is found that the ship detection probability and ship FAR decrease as the algorithm parameter M ($M \cdot \sigma_0$) increases, as expected. Meanwhile, it is also found that the higher the ship detection probability, the higher the ship FAR, when $M \cdot \sigma_0 \leq$

1.0 K. As aforementioned, the ship detection probability and ship FAR also increase as the parameter M decreases. However, a high detection probability with a low FAR is expected in ship detection. Thus, the algorithm parameter M should be carefully considered to get a high ship detection probability with a low ship FAR in the proposed algorithm, such as $M \cdot \sigma_0 = 1.3$
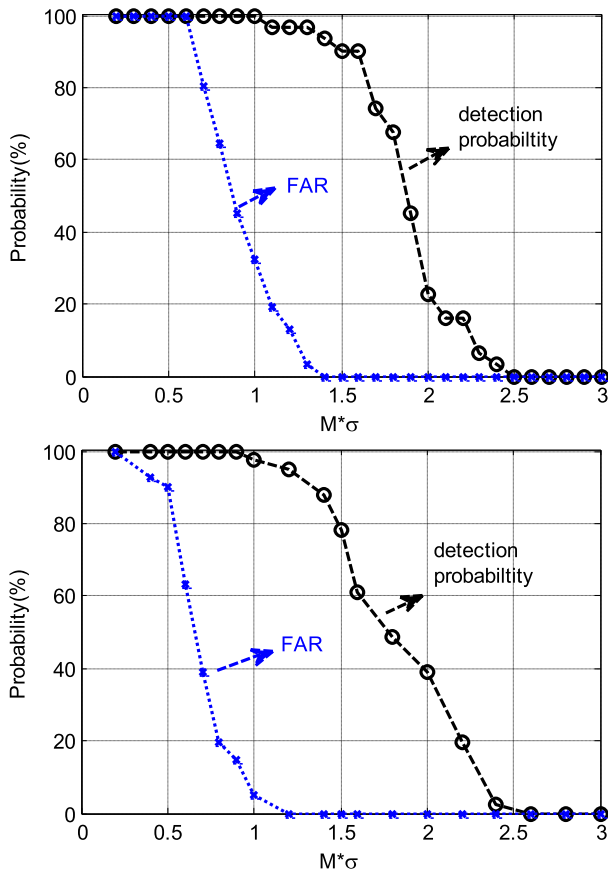
Fig. 20. Ship detection probability and ship FAR of two examples that Ship 2 (top) and Ship 3 (bottom) in Table I as a function of the algorithm parameter $M \cdot \sigma_0$.

K in Fig. 20. Given the experimental result, one consideration criterion of the algorithm parameter M is to maximize the ratio of the ship detection probability to the ship FAR with the ship detection probability higher than 50%.

VI. CONCLUSION

In this article, a ship detection and tracking algorithm is proposed for ship detection by the airborne PIMS, which comprises four steps that the observed TB map flag, the background-cancellation TB map, the ship flag map, and the ship tracking map. In comparison to the algorithm in [16], the proposed algorithm is devoted to ship tracking and ship heading. Meanwhile, the impacts of the algorithm parameter and the noises on the algorithm detection performance are analyzed and discussed. Numerical simulations and airborne experiments are also performed to demonstrate the practicability and assess the algorithm detection performance. Both numerical and experimental results indicate that the proposed algorithm is practical and the ships can be accurately detected and consecutively tracked by the algorithm. Meanwhile, the results also indicate the proposed algorithm can accurately estimate the ship heading and deal with the additional systematic errors. The results also demonstrate that the algorithm parameter M and the noises in (21) caused by the fluctuations of the aircraft have a non-negligible impact

on the ship detection performance. As a result, the "ship-free" observed TB maps should be carefully considered as the sea background TB map to improve the algorithm detection performance by reducing the noises in (21), which is caused by the fluctuations of the aircraft. In addition, the algorithm parameter M should also be carefully considered to get a high ship detection probability with a low ship FAR in the ship detection and tracking algorithm.

As mentioned in [16] and [23], ship wakes always exhibit a "hot" TB characteristic in the PIMI, and the "hot" TB characteristic of ship wakes has also been demonstrated by the airborne experiments in the article. As a result, the "hot" TB characteristic will be considered as another important characteristic to further improve the detection performance of the ship detection and tracking algorithm in further works.

ACKNOWLEDGMENT

REFERENCES

[1] Z. Liu, H. Wang, H. Weng, and L. Yang, "Ship rotated bounding box space for ship extraction from high-resolution optical satellite images with complex backgrounds," *IEEE Geosci. Remote Sens. Lett.*, vol. 13, no. 8, pp. 1074–1078, Aug. 2016.

[2] F. Yang, Q. Xu, and B. Li, "Ship detection from optical satellite images based on saliency segmentation and structure-LBP feature," *IEEE Geosci. Remote Sens. Lett.*, vol. 14, no. 5, pp. 602–606, Mar. 2017.

[3] G. K. Høye, T. Eriksen, B. J. Meland, and B. Narheim, "Space-based AIS for global maritime traffic monitoring," *Acta Astronautica*, vol. 62, no. 2–3, pp. 240–245, Feb. 2008.

[4] M. D. Graziano, D.'E. Marco, and E. Razzano, "Constellation analysis of an integrated AIS/remote sensing spaceborne system for ship detection," *Adv. Space Res.*, vol. 50, no. 3, pp. 351–362, Aug. 2012.

[5] C. Zhu, H. Zhou, R. Wang, and J. Guo, "A novel hierarchical method of ship detection from spaceborne optical image based on shape and texture features," *IEEE Trans. Geosci. Remote Sens.*, vol. 48, no. 9, pp. 3446–3456, Sep. 2010.

[6] J. Lu, Y. He, H. Li, and F. Lu, "Detecting small target of ship at sea by infrared image," in *Proc. IEEE Int. Conf. Automat. Sci. Eng.*, Oct. 2006, pp. 165–169.

[7] H. Wang, Z. Zou, Z. Shi, and B. Li, "Detecting ship targets in spaceborne infrared image based on modeling radiation anomalies," *Infrared Phys. Technol.*, vol. 85, pp. 141–146, Sep. 2017.

[8] S. Brusch, S. Lehner, T. Fritz, M. Soccorsi, A. Soloviev, and B. van Schie, "Ship surveillance with TerraSAR-X," *IEEE Trans. Geosci. Remote Sens.*, vol. 49, no. 3, pp. 1092–1103, Mar. 2011.

[9] Y. Wang and H. Liu, "A hierarchical ship detection scheme for high-resolution SAR images," *IEEE Trans. Geosci. Remote Sens.*, vol. 50, no. 10, pp. 4173–4184, Oct. 2012.

[10] J. Tang, C. Deng, G. B. Huang, and B. Zhao, "Compressed-domain ship detection on spaceborne optical image using deep neural network and extreme learning machine," *IEEE Trans. Geosci. Remote Sens.*, vol. 53, no. 3, pp. 1174–1185, Mar. 2015.

[11] F. Yang, Q. Xu, and B. Li, "Ship detection from optical satellite images based on saliency segmentation and structure-LBP feature," *IEEE Geosci. Remote Sens. Lett.*, vol. 14, no. 5, pp. 602–606, Mar. 2017.

[12] R. Appleby, D. G. Gleed, R. N. Anderton, and A. H. Lettington, "High-performance passive millimeter-wave imaging," *Opt. Eng.*, vol. 32, no. 6, pp. 1370–1373, May 1993.

[13] L. Yujiri, M. Shoucri, and P. Moffa, "Passive millimeter-wave imaging," *IEEE Microw. Mag.*, vol. 4, no. 3, pp. 39–50, Sep. 2003.

[14] G. Yang, B. Li, S. Ji, F. Gao, and Q. Xu, "Ship detection from optical satellite images based on sea surface analysis," *IEEE Geosci. Remote Sens. Lett.*, vol. 11, no. 3, pp. 641–645, Mar. 2014.

[15] A. R. Harvey and R. Appleby, "Passive mm-wave imaging from UAVs using aperture synthesis," *Aeronaut. J.*, vol. 107, no. 1068, pp. 87–98, Feb. 2003.

[16] H. Lu *et al.*, "Ship detection by an airborne passive interferometric microwave sensor (PIMS)," *IEEE Trans. Geosci. Remote Sens.*, vol. 58, no. 4, pp. 2682–2694, Apr. 2020.

[17] Y. A. Pirogov, "Passive millimeter-wave imaging," *Radiophys. Quantum Electron.*, vol. 46, no. 8–9, pp. 594–603, Aug./Sep. 2003.

[18] Y. Sasaki, I. Asanuma, K. Muneyama, G. Naito, and T. Suzuki, "The dependence of sea-surface microwave emission on wind speed, frequency, incidence angle, and polarization over the frequency range from 1 to 40 GHz," *IEEE Trans. Geosci. Remote Sens.*, vol. GE-25, no. 2, pp. 138–146, Mar. 1987.

[19] J. Gourrion, S. Guimbard, M. Portabella, and R. Sabia, "Toward an optimal estimation of the SMOS antenna-frame systematic errors," *IEEE Trans. Geosci. Remote Sens.*, vol. 51, no. 9, pp. 4752–4760, Sep. 2013.

[20] M. A. Brown, F. Torres, I. Corbella, and A. Colliander, "SMOS calibration," *IEEE Trans. Geosci. Remote Sens.*, vol. 46, no. 3, pp. 646–658, Feb. 2008.

[21] H. Lu *et al.*, "A hybrid calibration method for aperture synthesis radiometers," *IEEE Geosci. Remote Sens. Lett.*, vol. 13, no. 5, pp. 651–655, May 2016.

[22] J. Gourrion, R. Sabia, M. Portabella, J. Tenerelli, S. Guimbard, and A. Camps, "Characterization of the SMOS instrumental error pattern correction over the ocean," *IEEE Geosci. Remote Sens. Lett.*, vol. 9, no. 4, pp. 793–797, Feb. 2012.

[23] N. A. Salmon, "Outdoor passive millimeter-wave imaging: Phenomenology and scene simulation," *IEEE Trans. Antennas Propag.*, vol. 66, no. 2, pp. 897–908, Feb. 2018.

[24] S. R. Vedrilla, "Calibration, validation and polarimetry in 2D aperture synthesis: Application to MIRAS," Ph.D. dissertation, Dept. Telecommun. Eng., Univ. Politècnica de Catalunya, Barcelona, Spain, 2005.

[25] E. Anterrieu and A. Khazaal, "Brightness temperature map reconstruction from dual-polarimetric visibilities in synthetic aperture imaging radiometry," *IEEE Trans. Geosci. Remote Sens.*, vol. 46, no. 3, pp. 606–612, Mar. 2008.

[26] C. S. Ruf, C. T. Swift, A. B. Tanner, and D. M. Le Vine, "Interferometric synthetic aperture microwave radiometry for the remote sensing of the Earth," *IEEE Trans. Geosci. Remote Sens.*, vol. 26, no. 5, pp. 597–611, Sep. 1988.